

# Tailoring Interfaces for Enhanced Methanol Production from Photoelectrochemical CO<sub>2</sub> Reduction

Bo Shang<sup>a,b,†</sup>, Fengyi Zhao<sup>c,†</sup>, Sa Suo<sup>c</sup>, Yuanzuo Gao<sup>a,b</sup>, Colton Sheehan<sup>e</sup>, Sungho Jeon<sup>d</sup>, Jing Li<sup>a,b</sup>, Conor L. Rooney<sup>a,b</sup>, Oliver Leitner<sup>a,b</sup>, Langqiu Xiao<sup>e</sup>, Hanqing Fan<sup>f</sup>, Menachem Elimelech<sup>f</sup>, Leizhi Wang<sup>b</sup>, Gerald J. Meyer<sup>g</sup>, Eric A. Stach<sup>d</sup>, Thomas E. Mallouk<sup>e</sup>, Tianquan Lian<sup>\*c</sup>, Hailiang Wang<sup>\*a,b</sup>

a. Department of Chemistry, Yale University, New Haven, Connecticut, 06520, USA

b. Energy Sciences Institute, Yale University, West Haven, Connecticut, 06516, USA

c. Department of Chemistry, Emory University, 1515 Dickey Drive, Atlanta, Georgia, 30322, United States

d. Department of Materials Science and Engineering, University of Pennsylvania, Philadelphia, Pennsylvania 19104, United States

e. Department of Chemistry, University of Pennsylvania, Philadelphia, PA 19104 USA

f. Department of Chemical and Environmental Engineering, Yale University, New Haven, CT, 06520-8286, USA

g. Department of Chemistry, University of North Carolina at Chapel Hill, Chapel Hill, North Carolina 27599, United States

Email: [tlian@emory.edu](mailto:tlian@emory.edu); [hailiang.wang@yale.edu](mailto:hailiang.wang@yale.edu)

†: equal contributions

## Abstract

Efficient and stable photoelectrochemical reduction of CO<sub>2</sub> into highly reduced liquid fuels remains a formidable challenge, which requires innovative semiconductor/catalyst interface to tackle. In this study, we introduce a strategy involving the fabrication of a silicon micropillar array structure coated with a superhydrophobic fluorinated carbon layer for the photoelectrochemical conversion of CO<sub>2</sub> into methanol. The pillars increase the electrode surface area, improve catalyst loading and adhesion without compromising light absorption, and help confine gaseous intermediates near the catalyst surface. The superhydrophobic coating passivates parasitic side reactions and further enhances local accumulation of reaction intermediates. Upon one-electron reduction of the molecular catalyst, the semiconductor/catalyst interface changes from adaptive to buried junctions, providing a sufficient thermodynamic driving force for CO<sub>2</sub> reduction. These structures together create a unique microenvironment for effective reduction of CO<sub>2</sub> to methanol, leading to a remarkable Faradaic efficiency reaching 20% together with a partial current density of 3.4 mA cm<sup>-2</sup>, surpassing the previous record based on planar silicon photoelectrodes by a notable factor of 17. This work demonstrates a new pathway for enhancing photoelectrocatalytic CO<sub>2</sub> reduction through meticulous interface and microenvironment tailoring, and sets a benchmark for both Faradaic efficiency and current density in solar liquid fuel production.

## Introduction

The reduction of carbon dioxide (CO<sub>2</sub>) into liquid fuels with renewable energy represents a promising solution to both combat greenhouse gas emissions and store renewable energy.<sup>1-2</sup> Photoelectrocatalysis has emerged as an efficient method to harness solar energy and facilitate CO<sub>2</sub> electroreduction at low applied voltages.<sup>3-6</sup> In a typical photoelectrocatalytic (PEC) CO<sub>2</sub> reduction process, a semiconductor absorbs light to generate excited electrons, which are transferred by a catalyst to CO<sub>2</sub>. Among the various semiconductor materials investigated, Si-based photocathodes have garnered attention due to their cost-effectiveness, solar light harvesting, and well-understood properties.<sup>7-8</sup> Molecular catalysts, particularly transition metal complexes, are viable options for catalyzing the CO<sub>2</sub> reduction reaction, offering high selectivity and tunable catalytic properties.<sup>9-11</sup> Previous studies have achieved successful CO<sub>2</sub> reduction to CO and formate using Si-based photocathodes combined with molecular catalysts.<sup>7, 12-13</sup> However, achieving efficient and stable PEC CO<sub>2</sub> reduction to more highly reduced liquid fuels remains an important challenge.<sup>14-16</sup>

In our prior work, we explored a TiO<sub>2</sub>-coated planar p-type Si substrate integrated with a cobalt phthalocyanine (CoPc)/graphene oxide (GO) hybrid catalyst via a molecular linker.<sup>15</sup> Although this photocathode demonstrated the ability to achieve six-electron reduction of CO<sub>2</sub> to methanol with a Faradaic efficiency (FE) of 8%, the current density and stability were limited, likely due to the relatively low catalytic performance of GO/CoPc and weak interactions with the Si substrate. To improve the PEC performance, successful integration of a better optimized catalyst on Si is desired and requires addressing several challenges in fundamental energy research that include: 1) stabilization of the catalyst on the Si surface through covalent linking or self-assembly; 2) identification of the ideal catalyst surface loading for optimal catalysis and minimal light absorption; 3) passivation of the native Si surface to inhibit hydrogen evolution reaction (HER); 4) tailoring of the interfacial energetics to provide the thermodynamic driving force necessary for rapid interfacial electron transfer; 5) creation of a hydrophobic interfacial environment to tailor reaction selectivity towards methanol. These five challenges can be overcome through critical control of the interface between the Si light absorber and the molecular catalyst.<sup>17</sup>

In this article, we report the achievement of PEC CO<sub>2</sub> reduction to methanol with over 20% FE, a remarkable partial photocurrent density of 3.4 mA cm<sup>-2</sup>, and a high turnover frequency (TOF) of 1.5 s<sup>-1</sup>. This stands as the highest performance reported to date for any molecular catalyst-based photoelectrode. The enhancement in performance was realized by designing the semiconductor/catalyst interface and tailoring the electrode microenvironment, which plays a critical role in optimizing the CO<sub>2</sub> reduction to methanol cascade. We fabricated the p-type Si substrate surface into an array of micropillars, which enabled effective integration of a carbon nanotube/amine-substituted CoPc (CNT/CoPc-NH<sub>2</sub>) catalyst without sacrificing light absorption as well as improved retention of the key CO intermediate. This Si micropillar

array (SMA) photoelectrode yielded a 1.6-fold increase in total current density and a 1.5-fold increase in  $FE_{\text{methanol}}$  compared to a previously reported planar Si electrode with the GO/CoPc catalyst.<sup>15</sup> We further introduced a superhydrophobic carbon fluoride ( $CF_x$ ) coating on the SMA substrate to enhance the conversion of the gaseous reactant and intermediate. This microenvironment led to another 2-fold increase in  $FE_{\text{methanol}}$  and more remarkably, an additional 7-fold increase in the methanol partial current density. *In situ* Raman spectroscopy revealed  $\sim 300$  mV of photovoltage from SMA and a transition from adaptive to buried semiconductor/catalyst junctions with negative applied potential, further deepening our mechanistic understanding of the SMA-CNT/CoPc-NH<sub>2</sub> interface.

## Results and Discussion

The SMA structure with a pillar diameter of 3  $\mu\text{m}$ , a pillar height of 18  $\mu\text{m}$ , and a pitch of 10  $\mu\text{m}$  was fabricated through photolithography and dry etching (Figure 1a, Figure S1). Following the etching step, a thin  $CF_x$  layer was coated on SMA using an octafluorocyclobutane ( $C_4F_8$ ) plasma. Subsequently, the CNT/CoPc-NH<sub>2</sub> catalyst was drop-casted onto the SMA- $CF_x$  substrate (Figure 1b, Figure S2). Due to the hydrophobic nature of the SMA- $CF_x$  surface, the CNT/CoPc-NH<sub>2</sub> catalyst exhibits a preference for adhering to the top and sides of the Si pillars rather than the flat basal plane of the substrate (Figure 1c-e), likely as a result of surface tension of the catalyst ink. This distinct assembly pattern leaves approximately 90% of the geometrical area free of the strongly absorbing black CNTs for more optimal solar light harvesting by the Si substrate.

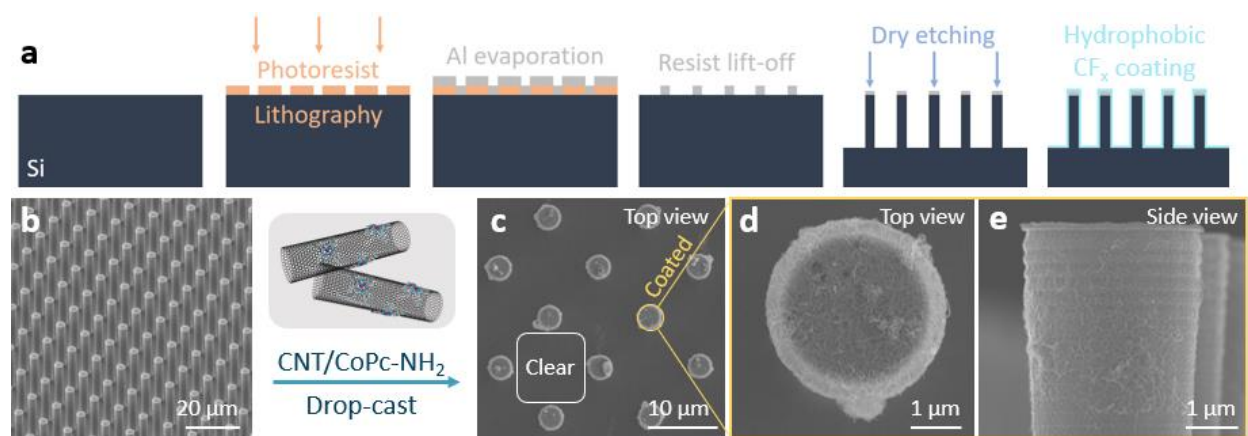


**Figure 1.** (a) SMA fabrication and  $CF_x$  coating. (b) SEM image of SMA- $CF_x$ . (c) SEM image of SMA- $CF_x$  coated with CNT/CoPc-NH<sub>2</sub> catalyst. (d-e) Top-view and side-view SEM images of a single SMA- $CF_x$  pillar coated with CNT/CoPc-NH<sub>2</sub>.

To directly probe how the quasi-Fermi level of the CNT/CoPc-NH<sub>2</sub> catalyst changes with applied potential under illumination, the SMA-CF<sub>x</sub>-CNT/CoPc-NH<sub>2</sub> photoelectrode was characterized by *in situ* Raman spectroscopy in CO<sub>2</sub>-saturated 0.1 M aqueous KHCO<sub>3</sub> (pH 6.8) using a 632.8 nm He-Ne laser as both a Raman probe and an illumination source.<sup>18</sup> A representative set of potential dependent Raman spectra is shown in Figure 2a. Linear sweep voltammetry (LSV) at a scan rate of 1.7 mV/s from 0.625 to -0.375 V (Figure 2b) vs the reversible hydrogen electrode (RHE, all potentials in this work are referenced to RHE unless otherwise stated) were conducted in the dark and in the light, the latter being concurrent with Raman spectrum acquisition. Resonance Raman features of CoPc-NH<sub>2</sub> were observed at 755, 1458, and 1543 cm<sup>-1</sup> (red shade in Figure 2a).<sup>19-21</sup> The peaks at 1334, 1585, and 1617 cm<sup>-1</sup> correspond to CNT's D, G<sup>-</sup>, and G<sup>+</sup> bands (gray shade in Figure 2a), respectively.<sup>22-23</sup> Our initial focus was to monitor the resonant Raman peaks of CoPc-NH<sub>2</sub> as a function of applied potential, whose intensity is known to decrease upon one-electron reduction of the CoPc-NH<sub>2</sub> molecule.<sup>19-20</sup> As the applied potential is polarized toward the negative direction, the CoPc-NH<sub>2</sub> resonances start to decrease in magnitude at 0.3 V, and the decrease levels off after the potential reaches 0 V (Figure 2c), suggesting that the CoPc-NH<sub>2</sub> molecules undergo one-electron reduction in this potential range. A photoelectrochemical reduction wave was consistently observed that reaches a peak current at 0.05 V in the same potential range of the LSV measurements (Figure 2b). Starting at 0 V, a new Raman peak was observed at 746 cm<sup>-1</sup> (green shade in Figure 2a, Figure S3), which is attributed to the reduced CoPc-NH<sub>2</sub>. In a control experiment, the electrochemical reduction of CNT/CoPc-NH<sub>2</sub> deposited on a degenerately doped n-type SMA-CF<sub>x</sub> (n<sup>+</sup>-SMA-CF<sub>x</sub>) substrate was quantified (Figure S4). The resonant Raman peaks of CoPc-NH<sub>2</sub> did not reach their lowest intensity until about -0.3 V, which, in comparison with the corresponding SMA-CF<sub>x</sub>-CNT/CoPc-NH<sub>2</sub> results (Figure 2c), suggests a 300 mV of photovoltage, i.e., quasi-Fermi-level splitting, for the p-type SMA electrode.

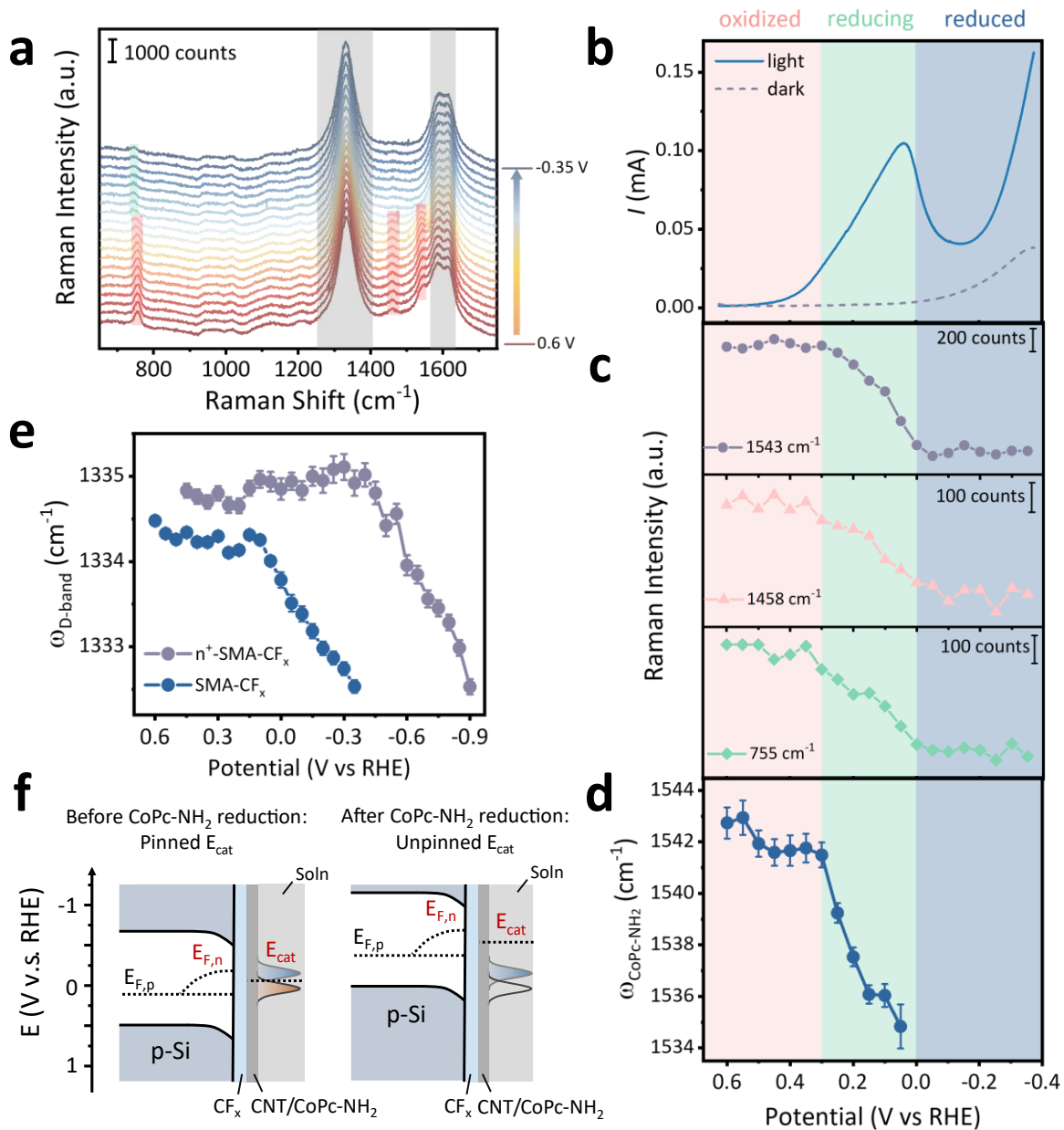


**Figure 2.** (a) *In situ* Raman spectra of CNT/CoPc-NH<sub>2</sub> on SMA-CF<sub>x</sub> from 0.625 V to -0.375 V under 632.8 nm illumination. (b) Linear sweep voltammograms of SMA-CF<sub>x</sub>-CNT/CoPc-NH<sub>2</sub> measured in the dark and during *in situ* Raman measurement. (c) One-electron reduction of CoPc-NH<sub>2</sub> tracked by changes in resonance Raman intensity. Potential-dependent Raman vibrational frequencies of (d) CoPc-NH<sub>2</sub> 1543  $\text{cm}^{-1}$  peak and (e) CNT D band. (f) Proposed band diagram at SMA-CF<sub>x</sub>-CNT/CoPc-NH<sub>2</sub>-solution interfaces. The electrode was tested after pre-conditioning the electrode at -0.5 V for 10 min under 150  $\text{mW cm}^{-2}$  Xe lamp irradiation. The red, blue, and green shaded potential regions in (b), (c), and (d) indicate the potential

ranges of oxidized, reduced, and mixed CoPc-NH<sub>2</sub> species, respectively, as determined from the Raman data shown in (c).

Further details about the CNT/CoPc-NH<sub>2</sub> catalyst were obtained through fitting of the CNT D, G<sup>+</sup>, and G<sup>-</sup> bands as well as the 1458 and 1543 cm<sup>-1</sup> peaks of CoPc-NH<sub>2</sub> (Figure S5). The frequency of the CoPc-NH<sub>2</sub> 1543cm<sup>-1</sup> peak ( $\omega_{\text{CoPc-NH}_2}$ ) exhibits intriguing potential-dependent behavior. At potentials above 0.3 V the frequency was unchanged and decreased continuously with increasingly reducing potential in the 0.3-0 V range (Figure 2d). The measured  $\omega_{\text{CoPc-NH}_2}$  shift is attributed to the potential-dependent electric field at the CNT/CoPc-NH<sub>2</sub>-electrolyte interface that affects the CoPC-NH<sub>2</sub> frequency through a Stark-like effect, or the electro-inductive effect on CoPc-NH<sub>2</sub> molecules induced by a change in the CNT Fermi level.<sup>24-26</sup> Of the three observed vibrational modes of CoPc-NH<sub>2</sub>, the 1543 cm<sup>-1</sup> peak, assigned to the C <sub>$\alpha$</sub> -N <sub>$\beta$</sub> -C <sub>$\alpha$</sub>  bridging bond displacement, was the only one that displayed a significant potential-dependent frequency shift. This may be resulted from the macrocycle plane's rotation along the C <sub>$\alpha$</sub> -N <sub>$\beta$</sub> -C <sub>$\alpha$</sub>  bridge that generates a dipole moment perpendicular to the CNT surface.<sup>26</sup> The other two modes, however, mainly generate dipole moments within the molecular plane.<sup>21, 27</sup>

The frequency of the CNT D band ( $\omega_{\text{D-band}}$ ) has been shown to be sensitive to the Fermi level of the material and can be used as a reporter of chemical and electrochemical doping.<sup>23, 28-29</sup> Interestingly,  $\omega_{\text{D-band}}$  shows a potential-dependent behavior similar to the 1543 cm<sup>-1</sup> peak of CoPc-NH<sub>2</sub>. As the applied potential is swept cathodically from 0.625 V to -0.375 V,  $\omega_{\text{D-band}}$  remains constant until ~0.1 V and then decreases (Figure 2e). We attribute this to a shift of the CNT quasi-Fermi-level at ~0.1V for CNT/CoPc-NH<sub>2</sub> on SMA-CF<sub>x</sub> under photoelectrochemical conditions. For CNT/CoPc-NH<sub>2</sub> integrated with n<sup>+</sup>-SMA-CF<sub>x</sub>, a similar potential-dependent  $\omega_{\text{D-band}}$  trend was observed, but the onset of  $\omega_{\text{D-band}}$  frequency shift occurs at -0.3 V (grey trace in Figure 2e). It is worth noting that although the shift of  $\omega_{\text{D-band}}$  reports on change of CNT Fermi level, it is difficult to establish a universal calibration curve that relates the  $\omega_{\text{D-band}}$  value to the Fermi level (Figure S6 and Table S1) because the D band frequency are not only sensitive to the electric field but also to solution microenvironment factors such as chemisorption of electrolyte ions and local pH changes.<sup>28, 30-31</sup>

Based on the above analysis, we propose the following properties for the SMA-CF<sub>x</sub>-CNT/CoPc-NH<sub>2</sub>-solution junction. As summarized in Figure 2f, the potentiostat controls the hole Fermi-level of Si (E<sub>F,p</sub>); the quasi-Fermi-level of electrons (E<sub>F,n</sub>) shifts to higher energy upon photogeneration and separation of electrons; the Fermi-level of CNT and the attached CoPc-NH<sub>2</sub> molecules equilibrate with each other, denoted as E<sub>cat</sub>. From the Si flat-band potential to 0.1 V (left panel of Figure 2f), E<sub>cat</sub> is pinned by the one-

electron reduction potential of CoPc-NH<sub>2</sub>, which means that the applied potential mainly drops on the semiconductor side, providing the electric field needed to separate the photogenerated charge carriers and generating a ~300 mV photovoltage to reduce the CoPc-NH<sub>2</sub> molecules. When the applied potential becomes more negative than 0.1 V (right panel of Figure 2f), E<sub>cat</sub> is unpinned as the molecules are reduced. In this potential region, the semiconductor band bending and the height of the semiconductor-catalyst barrier remain constant, irrespective of the applied potential. The applied potential change ( $\Delta E_{F,p}$ ) directly shifts E<sub>cat</sub> towards more negative potential. The junction properties in terms of pinned and unpinned E<sub>cat</sub> are also known as ‘adaptive’ and ‘buried’ junctions, respectively, according to the literature.<sup>32-35</sup> The formation of the buried junction results in an electrostatic potential drop across the solution double layer, which could render a suitable microenvironment for CO<sub>2</sub> reduction at more negative potentials. Our result suggests efficient electron tunneling from SMA to CNT/CoPc-NH<sub>2</sub> in this architecture.

The performance of the fabricated photoelectrode for PEC CO<sub>2</sub> reduction was evaluated in CO<sub>2</sub>-saturated 0.1 M aqueous KHCO<sub>3</sub> using an H-cell with a quartz window under the illumination of an Xe lamp (150 mW cm<sup>-2</sup>, 400 nm cutoff), as depicted in Figure 3a. All constant-potential photoelectrolysis experiments were conducted after pre-conditioning the electrode at -0.5 V under illumination for 10 min. The current increases and then stabilizes during the pre-conditioning (Figure S7), which is possibly due to the dissolution of the insulating native oxide layer on Si. *In situ* Raman spectroscopy measurement of unconditioned SMA-CF<sub>x</sub>-CNT/CoPc-NH<sub>2</sub> shows reduction of CoPc-NH<sub>2</sub> and electron doping of CNTs similar to that on the pre-conditioned photoelectrode but at more cathodic potentials (Figure S8). By comparing the CoPc-NH<sub>2</sub> reduction and  $\omega_{D\text{-band}}$  shifting potentials between these two conditions, we find that the pre-conditioning could reduce the interfacial potential loss by about 200 mV, likely by reducing the surface oxide or passivating the surface states on Si and thus decreasing the interfacial resistance. Under -0.7 V applied potential (after pre-conditioning), the SMA-CF<sub>x</sub>-CNT/CoPc-NH<sub>2</sub> photocathode delivers a methanol FE of 21% and a CO FE of 37%, accompanied by a total photocurrent of 16.6 mA cm<sup>-2</sup> (Figure 3b). A photovoltage of ~350 mV is gained from the Si substrate, as inferred from the maximum-FE<sub>methanol</sub> potential difference with vs without illumination (Figure S9), which matches the *in situ* Raman results (Figure 2c, Figure S4). The stability of SMA-CF<sub>x</sub>-CNT/CoPc-NH<sub>2</sub> was evaluated under the constant-current mode with a photocurrent of 15 mA cm<sup>-2</sup> (Figure 3c). In the first 20 min, the applied potential drops continuously, which is similar to the activation observed in the pre-conditioning step under the constant-potential mode. After that, a stable FE of ~20% for methanol is achieved and maintained for 2 h. Subsequently, FE<sub>methanol</sub> decreases to 6%, accompanied by an increase in the partial current density of H<sub>2</sub>, which may be attributed to the exposure of the Si surface to the electrolyte.

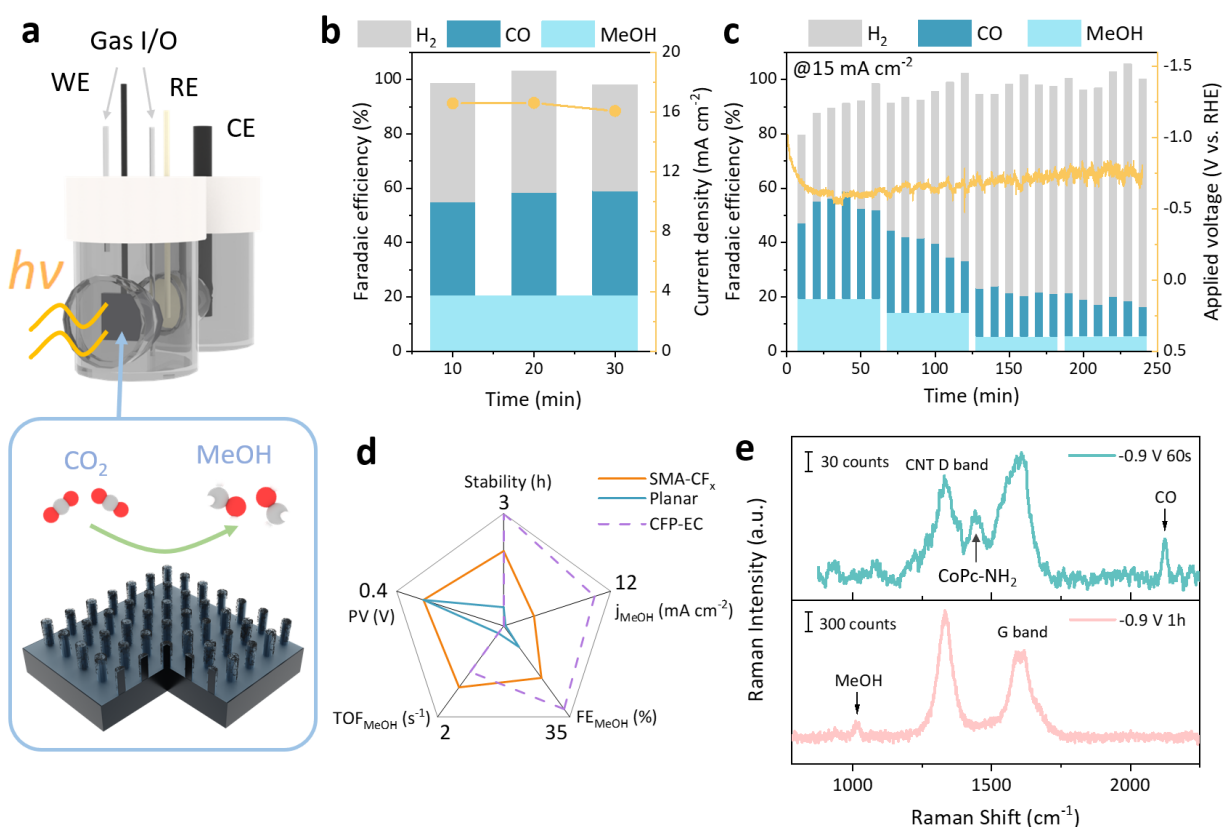


**Figure 3.** PEC CO<sub>2</sub> reduction performance of SMA-CF<sub>x</sub>-CNT/CoPc-NH<sub>2</sub> in 0.1 M aqueous KHCO<sub>3</sub> under illumination. (a) PEC cell structure. (b) Total photocurrent and product distribution at -0.7 V. CO and H<sub>2</sub> were sampled every 10 min, whereas methanol concentration was measured after the 30 min reaction to report its average FE. (c) Stability test at constant photocurrent of 15 mA cm<sup>-2</sup>, showing the applied potential needed to maintain the constant photocurrent (yellow line, right axis) and the FEs for H<sub>2</sub>, CO and methanol (vertical bars, left axis) as a function of time. (d) Performance comparison with GO/CoPc-functionalized planar Si (under illumination), and CNT/CoPc-NH<sub>2</sub> deposited on carbon fiber paper for electrocatalysis (CFP-EC, electrolysis without illumination). (e) *In situ* Raman measurements at -0.9 V at 60 s (top) and 1 h (bottom) into photoelectrolysis at -0.9 V, showing generated CO and methanol.

Comparison of performance for CO<sub>2</sub> reduction to methanol, in terms of stability, partial current density, FE, TOF, and photovoltage, is made between different CoPc-based (photo)electrodes (Figure 3d). The SMA-CF<sub>x</sub>-CNT/CoPc-NH<sub>2</sub> photoelectrode has arguably the best overall performance. It exhibits a similar photovoltage of ~350 mV but 3, 17, and 4 times higher FE, methanol production rate, and stable operation time, respectively, than our prior generation of photoelectrodes based on planar Si and the GO/CoPc

catalyst.<sup>15</sup> Compared with the state-of-the-art electrode of CNT/CoPc-NH<sub>2</sub> deposited on CFP (Figure S10), the SMA-CF<sub>x</sub>-CNT/CoPc-NH<sub>2</sub> photoelectrode has the advantage of improved overpotential because of the photovoltage, but is about 1.3 times lower in FE and 3 times lower in partial current density (Figure 3d).<sup>9</sup> The lower methanol selectivity and production rate may be attributed to lower catalyst loading (0.1 mg cm<sup>-2</sup> on SMA vs 0.4 mg cm<sup>-2</sup> on CFP) and less effective CO<sub>2</sub> mass transport (the hydrophobic CFP substrate resembles a gas diffusion electrode). Both are limitations that need to be solved in future work to further improve the PEC performance. Interestingly, the TOF for methanol production on SMA-CF<sub>x</sub>-CNT/CoPc-NH<sub>2</sub> reaches approximately 1.5 s<sup>-1</sup>, largely comparable to that achieved in CNT/CoPc-NH<sub>2</sub>-catalyzed electrolysis (1.0 s<sup>-1</sup>) if the different catalyst loadings are taken into consideration. CO<sub>2</sub> reduction intermediates and products are also detected by Raman spectroscopy as shown in Figure 3e. 60 s into photoelectrolysis under -0.9 V applied potential, a peak at 2120 cm<sup>-1</sup> evolves (green, upper panel), confirming the formation of free CO bubbles on the surface.<sup>36</sup> A peak at 1015 cm<sup>-1</sup> appears after 1 h of reaction and product accumulation (pink, lower panel). This peak is assigned to methanol's C-O stretching (Figure S11),<sup>37</sup> confirming the generation of methanol as a product. The 2120 cm<sup>-1</sup> CO peak is not detected in this spectrum, likely because loosely bound CO bubbles detach from the electrode.

The improved methanol production performance of the SMA-CF<sub>x</sub>-CNT/CoPc-NH<sub>2</sub> photoelectrode is a result of the micropillar array structure and the CF<sub>x</sub> coating. The SMA-CNT/CoPc-NH<sub>2</sub> photoelectrode (without CF<sub>x</sub>) shows 1.5 times the FE and 2.3 times the partial current density of the planar Si-GO/CoPc electrode (Figure 4a), demonstrating the effect of the SMA surface. Considering that CO is the key reaction intermediate on the CO<sub>2</sub>-to-methanol pathway that easily desorbs from the CoPc catalytic site,<sup>38-40</sup> we hypothesize that the micropillar array structure can help retain CO micro-bubbles between the pillars and thus enhance their further reduction to generate methanol. This hypothesis is supported by our simulation results showing that the micropillar array structure can retain over 1.5 times the local CO concentration compared to the planar surface under identical CO generation fluxes (Figure S12). This hypothesis is also consistent with our experimental observation that, the height and pitch of the micropillar array influence methanol selectivity and photocurrent. Considerably lower FE<sub>methanol</sub> and slightly lower total current density are observed for SMA with a shorter pillar height of 7 μm (Figure S13a, b). This may be due to reduced CO trapping capability and lower electrode surface area. A larger pillar height of 36 μm does not seem to affect methanol production much but significantly increase the HER rate likely because of a larger area of exposed Si surface (Figure S13c, d).<sup>8, 15, 41</sup> For a similar reason, a smaller pitch of 8 μm also elevates H<sub>2</sub> evolution (Figure S13a, c).

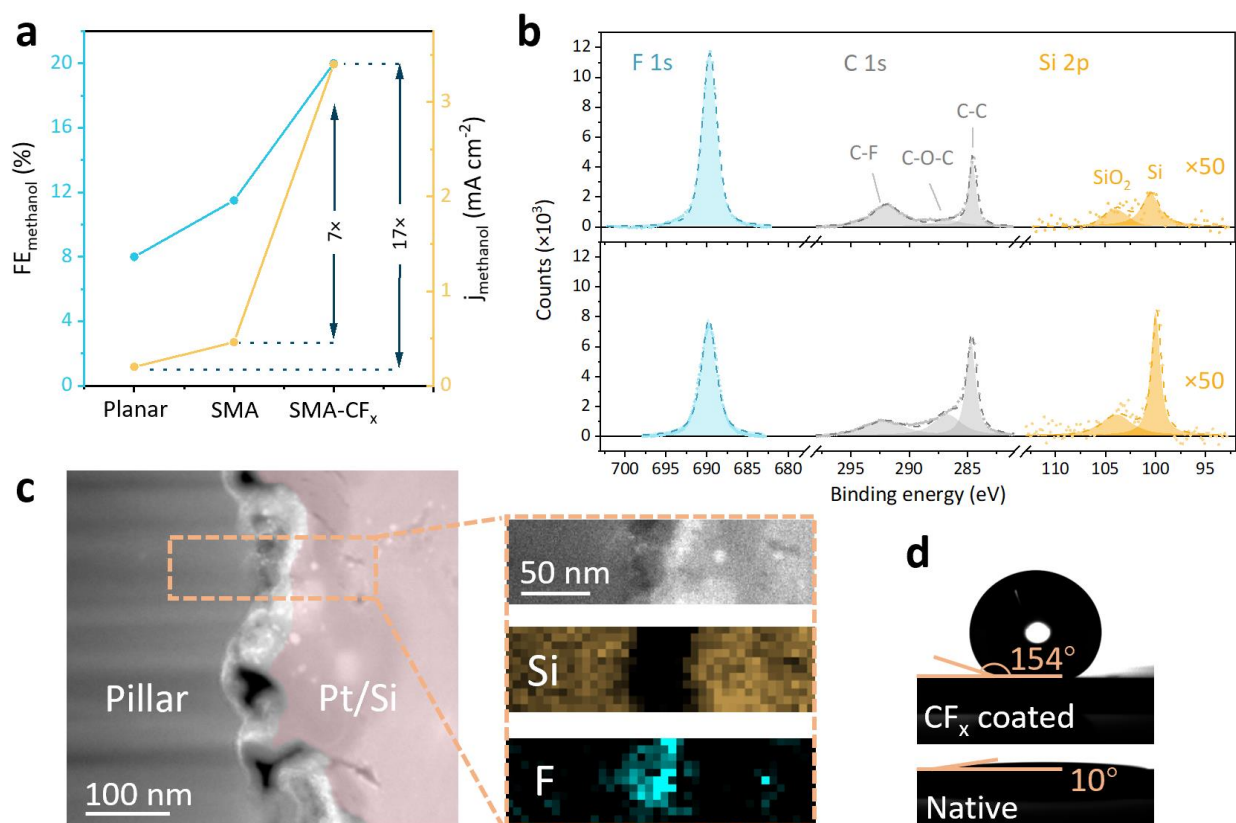


**Figure 4.** (a) Comparison of methanol selectivity and partial current density between SMA-CF<sub>x</sub>-CNT/CoPc-NH<sub>2</sub> (noted as SMA-CF<sub>x</sub>), SMA-CNT/CoPc-NH<sub>2</sub> (noted as SMA), and planar Si-TiO<sub>2</sub>-GO/CoPc (noted as Planar). (b) XPS spectra of SMA-CF<sub>x</sub>-CNT/CoPc-NH<sub>2</sub> before (upper panel) and after (lower panel) 4 h of PEC CO<sub>2</sub> reduction. (c) Cross-section STEM image of a single Si pillar, and STEM-EDS mapping of the boxed area. Pt/Si (false colored) was deposited onto the pillar sidewall to prepare the thin slice with FIB. (d) Contact angle measurements on SMA-CF<sub>x</sub> and SMA.

The CF<sub>x</sub> coating is also key to the enhanced PEC performance. X-ray photoelectron spectroscopy (XPS) successfully detected F and F-bonded C together with little Si (Figure 4b, upper panel), confirming the presence of CF<sub>x</sub> on the photoelectrode surface. To characterize the thickness and uniformity of the CF<sub>x</sub> layer, we used focused ion beam (FIB) to slice a thin layer (approximately 100 nm thick) off a pillar, as illustrated in Figure 4c and Figure S14. Scanning transmission electron microscopy (STEM) and energy-dispersive X-ray spectroscopy (EDS) were performed on the slice. A continuous F-containing layer with an average thickness of ~40 nm was observed (Figure 4c, Figure S15), suggesting that a CF<sub>x</sub> layer of the same thickness effectively covers the Si surface. With this coating, the SMA-CF<sub>x</sub> substrate exhibits

superhydrophobic properties with an ultrahigh contact angle of  $154^\circ$  with water, while the  $\text{CF}_x$ -free SMA (native oxide surface) shows a low contact angle of only  $10^\circ$  (Figure 4d, Figure S16, Video S1). Incorporation of  $\text{CF}_x$  into the SMA-CNT/CoPc-NH<sub>2</sub> structure increases CO<sub>2</sub> reduction current by 4 times and FE<sub>methanol</sub> by 1.8 times, leading to a 7-fold increase in methanol production rate (Figure 4a, Figure S13a). In a control experiment, a SMA-TiO<sub>2</sub>-CNT/CoPc-NH<sub>2</sub> photoelectrode exhibits a lower photocurrent ( $\sim 7 \text{ mA cm}^{-2}$ ), a lower methanol FE (14%), and a much higher H<sub>2</sub> FE (71%) than SMA-CF<sub>x</sub>-CNT/CoPc-NH<sub>2</sub> (Figure S17). This comparison reflects the roles of the hydrophobic  $\text{CF}_x$  layer. It can facilitate CO<sub>2</sub> mass transport, enhance CO retention, and suppress electrolyte penetration into the interspace of the micropillars, leading to improved CO<sub>2</sub> reduction to methanol and suppressed H<sub>2</sub> evolution.<sup>42</sup>

As the methanol production performance of the SMA-CF<sub>x</sub>-CNT/CoPc-NH<sub>2</sub> photoelectrode starts to decay after 2 h of operation (Figure 3c), we further examined a used photoelectrode (after 4 h of PEC test at  $15 \text{ mA cm}^{-2}$ ) to understand the deactivation. Compared to the fresh photoelectrode, the deactivated photoelectrode has considerably less F and more Si on the surface as revealed by XPS (Figure 4b, Table S2), indicating that the  $\text{CF}_x$  coating layer has degraded after the long-term PEC test. This change in surface composition can explain the observed deactivation behavior. The degradation of the  $\text{CF}_x$  layer leads to lowered surface hydrophobicity, which lessens CO<sub>2</sub> reduction to methanol. On the other hand, the newly exposed Si surface facilitates HER.<sup>8, 15, 41</sup> We note that suppressing HER on Si photoelectrodes, especially during long-term operation, remains challenging. It is limited by the tradeoff between catalyst coverage/loading and light absorption as well as the durability of the surface passivation layer under reaction conditions. The highly reducing condition required for methanol production is a big threat to traditional metal oxide passivation layers like TiO<sub>2</sub><sup>15</sup>, and even  $\text{CF}_x$  is not adequate. Future work is needed to solve this problem.<sup>43</sup>

## Conclusion

In conclusion, our study successfully showcases the effectiveness of microenvironment and interface tailoring on Si-based CO<sub>2</sub> reduction photocathodes, leading to a remarkable FE of over 20% for methanol production with record-high partial current density. The incorporation of the micropillar array structure and the superhydrophobic  $\text{CF}_x$  coating plays a crucial role in enhancing retention of the CO intermediate, consequently improving the selectivity towards the deeply reduced methanol product. The unique Si-molecular catalyst buried junction efficiently converts absorbed photon energy into chemical driving force for CO<sub>2</sub> reduction. This work pioneers a route for microenvironment tailoring on semiconductor surfaces and establishes a new benchmark for PEC CO<sub>2</sub> reduction to liquid fuel using molecular catalysts. The

insights gained from this research hold promise for driving further developments in the quest for sustainable and efficient utilization of carbon emissions.

## Supporting Information

Materials, catalyst ink preparation, photoelectrode fabrication, photoelectrochemical measurements, characterization methods, numerical modeling method, and supplementary figures and tables.

## Acknowledgements

This work was solely supported as part of the Center for Hybrid Approaches in Solar Energy to Liquid Fuels (CHASE), an Energy Innovation Hub funded by the U.S. Department of Energy, Office of Science, Office of Basic Energy Sciences under Award Number DE-SC0021173. C.S. acknowledges an individual fellowship from the US National Science Foundation Graduate Research Fellowship Program (NSF GRFP, DGE-1845298). The electron microscopy was carried out at the Singh Center for Nanotechnology, which is supported by the NSF National Nanotechnology Coordinated Infrastructure Program under grant NNCI-2025608. Additional support to the Nanoscale Characterization Facility at the Singh Center has been provided by the Laboratory for Research on the Structure of Matter (MRSEC) supported by the National Science Foundation (DMR-1720530).

## References

1. Jordaan, S. M.; Wang, C., Electrocatalytic conversion of carbon dioxide for the Paris goals. *Nature Catalysis* **2021**, *4* (11), 915-920.
2. Wang, T.; Wang, Y.; Li, Y.; Li, C., The origins of catalytic selectivity for the electrochemical conversion of carbon dioxide to methanol. *Nano Res* **2023**, <https://doi.org/10.1007/s12274-023-5653-7>.
3. Kondratenko, E. V.; Mul, G.; Baltrusaitis, J.; Larrazábal, G. O.; Pérez-Ramírez, J., Status and perspectives of CO<sub>2</sub> conversion into fuels and chemicals by catalytic, photocatalytic and electrocatalytic processes. *Energy & environmental science* **2013**, *6* (11), 3112-3135.
4. Bhattacharjee, S.; Rahaman, M.; Andrei, V.; Miller, M.; Rodríguez-Jiménez, S.; Lam, E.; Pornrunroj, C.; Reisner, E., Photoelectrochemical CO<sub>2</sub>-to-fuel conversion with simultaneous plastic reforming. *Nature Synthesis* **2023**, *2* (2), 182-192.
5. Shan, B.; Vanka, S.; Li, T.-T.; Troian-Gautier, L.; Brennaman, M. K.; Mi, Z.; Meyer, T. J., Binary molecular-semiconductor p–n junctions for photoelectrocatalytic CO<sub>2</sub> reduction. *Nature Energy* **2019**, *4* (4), 290-299.
6. Rahaman, M.; Andrei, V.; Wright, D.; Lam, E.; Pornrunroj, C.; Bhattacharjee, S.; Pichler, C. M.; Greer, H. F.; Baumberg, J. J.; Reisner, E., Solar-driven liquid multi-carbon fuel production using a standalone perovskite–BiVO<sub>4</sub> artificial leaf. *Nature Energy* **2023**, *8* (6), 629-638.

7. Leung, J. J.; Warnan, J.; Ly, K. H.; Heidary, N.; Nam, D. H.; Kuehnel, M. F.; Reisner, E., Solar-driven reduction of aqueous CO<sub>2</sub> with a cobalt bis(terpyridine)-based photocathode. *Nature Catalysis* **2019**, 2 (4), 354-365.
8. Roh, I.; Yu, S.; Lin, C. K.; Louisia, S.; Cestellos Blanco, S.; Yang, P., Photoelectrochemical CO<sub>2</sub> Reduction toward Multicarbon Products with Silicon Nanowire Photocathodes Interfaced with Copper Nanoparticles. *Journal of the American Chemical Society* **2022**, 144 (18), 8002-8006.
9. Wu, Y.; Jiang, Z.; Lu, X.; Liang, Y.; Wang, H., Domino electroreduction of CO<sub>2</sub> to methanol on a molecular catalyst. *Nature* **2019**, 575 (7784), 639-642.
10. Zhang, X.; Wu, Z.; Zhang, X.; Li, L.; Li, Y.; Xu, H.; Li, X.; Yu, X.; Zhang, Z.; Liang, Y.; Wang, H., Highly selective and active CO<sub>2</sub> reduction electrocatalysts based on cobalt phthalocyanine/carbon nanotube hybrid structures. *Nat Commun* **2017**, 8 (1), 14675.
11. Shang, B.; Zhao, F.; Choi, C.; Jia, X.; Pauly, M.; Wu, Y.; Tao, Z.; Zhong, Y.; Harmon, N.; Maggard, P. A.; Lian, T.; Hazari, N.; Wang, H., Monolayer Molecular Functionalization Enabled by Acid–Base Interaction for High-Performance Photochemical CO<sub>2</sub> Reduction. *ACS Energy Letters* **2022**, 7 (7), 2265-2272.
12. Nandal, N.; Jain, S. L., A review on progress and perspective of molecular catalysis in photoelectrochemical reduction of CO<sub>2</sub>. *Coordin Chem Rev* **2022**, 451, 214271.
13. Chang, X.; Wang, T.; Yang, P.; Zhang, G.; Gong, J., The Development of Cocatalysts for Photoelectrochemical CO<sub>2</sub> Reduction. *Advanced Materials* **2019**, 31 (31), 1804710.
14. Wen, Z.; Xu, S.; Zhu, Y.; Liu, G.; Gao, H.; Sun, L.; Li, F., Aqueous CO<sub>2</sub> Reduction on Si Photocathodes Functionalized by Cobalt Molecular Catalysts/Carbon Nanotubes. *Angewandte Chemie International Edition* **2022**, 61, e202201086.
15. Shang, B.; Rooney, C. L.; Gallagher, D. J.; Wang, B. T.; Krayev, A.; Shema, H.; Leitner, O.; Harmon, N. J.; Xiao, L.; Sheehan, C.; Bottum, S. R.; Gross, E.; Cahoon, J. F.; Mallouk, T. E.; Wang, H., Aqueous Photoelectrochemical CO<sub>2</sub> Reduction to CO and Methanol over a Silicon Photocathode Functionalized with a Cobalt Phthalocyanine Molecular Catalyst. *Angewandte Chemie International Edition* **2023**, 62 (4), e202215213.
16. Wang, Q.; Pan, Z., Advances and challenges in developing cocatalysts for photocatalytic conversion of carbon dioxide to fuels. *Nano Res* **2022**, 15 (12), 10090-10109.
17. Yao, T.; An, X.; Han, H.; Chen, J. Q.; Li, C., Photoelectrocatalytic Materials for Solar Water Splitting. *Advanced Energy Materials* **2018**, 8 (21), 1800210.
18. Suo, S.; Sheehan, C.; Zhao, F.; Xiao, L.; Xu, Z.; Meng, J.; Mallouk, T. E.; Lian, T., Direct Vibrational Stark Shift Probe of Quasi-Fermi Level Alignment in Metal Nanoparticle Catalyst-Based Metal–Insulator–Semiconductor Junction Photoelectrodes. *Journal of the American Chemical Society* **2023**, 145 (26), 14260-14266.
19. Choi, C.; Zhao, F.; Hart, J. L.; Gao, Y.; Menges, F.; Rooney, C. L.; Harmon, N. J.; Shang, B.; Xu, Z.; Suo, S.; Sam, Q.; Cha, J. J.; Lian, T.; Wang, H., Synergizing Electron and Heat Flows in Photocatalyst for Direct Conversion of Captured CO<sub>2</sub>. *Angew. Chem. Int. Ed.* **2023**, 62, e202302152.
20. Jiang, S.; Chen, Z.; Chen, X.; Nguyen, D.; Mattei, M.; Goubert, G.; Van Duyne, R. P., Investigation of Cobalt Phthalocyanine at the Solid/Liquid Interface by Electrochemical Tip-Enhanced Raman Spectroscopy. *The Journal of Physical Chemistry C* **2019**, 123 (15), 9852-9859.
21. Liu, Z.; Chen, Z.-X.; Jin, B.; Zhang, X., Theoretical studies on the structures and vibrational spectra of Ni, Pd, and Pt phthalocyanines. *Vibrational Spectroscopy* **2011**, 56 (2), 210-218.
22. Dresselhaus, M. S.; Dresselhaus, G.; Saito, R.; Jorio, A., Raman spectroscopy of carbon nanotubes. *Physics Reports* **2005**, 409 (2), 47-99.
23. Filho, A. G. S.; Jorio, A.; Ge, G. S.; Dresselhaus, G.; Saito, R.; Dresselhaus, M. S., Raman spectroscopy for probing chemically/physically induced phenomena in carbon nanotubes. *Nanotechnology* **2003**, 14 (10), 1130.
24. Clark, M. L.; Ge, A.; Videla, P. E.; Rudshiteyn, B.; Miller, C. J.; Song, J.; Batista, V. S.; Lian, T.; Kubiak, C. P., CO<sub>2</sub> Reduction Catalysts on Gold Electrode Surfaces Influenced by Large Electric Fields. *J. Am. Chem. Soc.* **2018**, 140 (50), 17643-17655.

25. Heo, J.; Ahn, H.; Won, J.; Son, J. G.; Shon, H. K.; Lee, T. G.; Han, S. W.; Baik, M.-H., Electro-inductive effect: Electrodes as functional groups with tunable electronic properties. *Science* **2020**, *370* (6513), 214-219.
26. Shi, H.; Zhao, B.; Ma, J.; Bronson Jr, M. J.; Cai, Z.; Chen, J.; Wang, Y.; Cronin, M.; Jensen, L.; Cronin, S. B., Measuring Local Electric Fields and Local Charge Densities at Electrode Surfaces Using Graphene-Enhanced Raman Spectroscopy (GERS)-Based Stark-Shifts. *ACS Applied Materials & Interfaces* **2019**, *11* (39), 36252-36258.
27. Basova, T. V.; Kiselev, V. G.; Schuster, B.-E.; Peisert, H.; Chassé, T., Experimental and theoretical investigation of vibrational spectra of copper phthalocyanine: polarized single-crystal Raman spectra, isotope effect and DFT calculations. *Journal of Raman Spectroscopy* **2009**, *40* (12), 2080-2087.
28. Ott, A.; Verzhbitskiy, I. A.; Clough, J.; Eckmann, A.; Georgiou, T.; Casiraghi, C., Tunable D peak in gated graphene. *Nano Research* **2014**, *7* (3), 338-344.
29. Liu, J.; Li, Q.; Zou, Y.; Qian, Q.; Jin, Y.; Li, G.; Jiang, K.; Fan, S., The Dependence of Graphene Raman D-band on Carrier Density. *Nano Lett.* **2013**, *13* (12), 6170-6175.
30. Fu, W.; Nef, C.; Knopfmacher, O.; Tarasov, A.; Weiss, M.; Calame, M.; Schönenberger, C., Graphene Transistors Are Insensitive to pH Changes in Solution. *Nano Lett.* **2011**, *11* (9), 3597-3600.
31. Ang, P. K.; Chen, W.; Wee, A. T. S.; Loh, K. P., Solution-Gated Epitaxial Graphene as pH Sensor. *J. Am. Chem. Soc.* **2008**, *130* (44), 14392-14393.
32. Lin, F.; Boettcher, S. W., Adaptive semiconductor/electrocatalyst junctions in water-splitting photoanodes. *Nat. Mater.* **2014**, *13* (1), 81-86.
33. Nellist, M. R.; Laskowski, F. A. L.; Lin, F.; Mills, T. J.; Boettcher, S. W., Semiconductor–Electrocatalyst Interfaces: Theory, Experiment, and Applications in Photoelectrochemical Water Splitting. *Acc. Chem. Res.* **2016**, *49* (4), 733-740.
34. Lin, F.; Bachman, B. F.; Boettcher, S. W., Impact of Electrocatalyst Activity and Ion Permeability on Water-Splitting Photoanodes. *J. Phys. Chem. Lett.* **2015**, *6* (13), 2427-2433.
35. Mills, T. J.; Lin, F.; Boettcher, S. W., Theory and Simulations of Electrocatalyst-Coated Semiconductor Electrodes for Solar Water Splitting. *Physical Review Letters* **2014**, *112* (14), 148304.
36. Thibault, F.; Martinez, R. Z.; Domenech, J. L.; Bermejo, D.; Bouanich, J.-P., Raman and infrared linewidths of CO in Ar. *J. Chem. Phys.* **2002**, *117* (6), 2523-2531.
37. Hickstein, D. D.; Goldfarbmuren, R.; Darrah, J.; Erickson, L.; Johnson, L. A., Rapid, accurate, and precise concentration measurements of a methanol-water mixture using Raman spectroscopy. *OSA Continuum* **2018**, *1* (3), 1097-1110.
38. Wu, Y.; Liang, Y.; Wang, H., Heterogeneous Molecular Catalysts of Metal Phthalocyanines for Electrochemical CO<sub>2</sub> Reduction Reactions. *Accounts of Chemical Research* **2021**, *54* (16), 3149-3159.
39. Li, J.; Shang, B.; Gao, Y.; Cheon, S.; Rooney, C. L.; Wang, H., Mechanism-guided realization of selective carbon monoxide electroreduction to methanol. *Nature Synthesis* **2023**, *2*, 1194–1201.
40. Rooney, C.; Lyons, M.; Wu, Y.; Hu, G.; Wang, M.; Choi, C.; Gao, Y.; Chang, C.-W.; Brudvig, G.; Feng, Z.; Wang, H., Active Sites of Cobalt Phthalocyanine in Electrocatalytic CO<sub>2</sub> Reduction to Methanol. *Angewandte Chemie International Edition* **2023**, e202310623.
41. Kempler, P. A.; Richter, M. H.; Cheng, W.-H.; Brunschwig, B. S.; Lewis, N. S., Si Microwire-Array Photocathodes Decorated with Cu Allow CO<sub>2</sub> Reduction with Minimal Parasitic Absorption of Sunlight. *ACS Energy Letters* **2020**, *5* (8), 2528-2534.
42. Wakerley, D.; Lamaison, S.; Ozanam, F.; Menguy, N.; Mercier, D.; Marcus, P.; Fontecave, M.; Mougél, V., Bio-inspired hydrophobicity promotes CO<sub>2</sub> reduction on a Cu surface. *Nature Materials* **2019**, *18* (11), 1222-1227.
43. Deshmukh, A.; Boo, C.; Karanikola, V.; Lin, S.; Straub, A. P.; Tong, T.; Warsinger, D. M.; Elimelech, M., Membrane distillation at the water-energy nexus: limits, opportunities, and challenges. *Energy & Environmental Science* **2018**, *11* (5), 1177-1196.

## TOC Graphic

